PHYSICAL REVIEW A VOLUME 56, NUMBER 5 NOVEMBER 1997

Molecular effects on antiproton capture by H_2 and the states of $\overline{p}p$ formed

James S. Cohen*
Theoretical Division, Los Alamos National Laboratory, Los Alamos, New Mexico 87545

(Received 20 May 1997)

Complete five-body dynamical calculations of antiproton ($\overline{p}$) capture by the hydrogen molecule (H_2) have been carried out using a generalization of the Kirschbaum-Wilets method (belonging to a class of quasiclassical methods sometimes called fermion molecular dynamics). The differences between capture by H_2 and the H atom are found to be dramatic. The effects due to the two-center structure, rotational motions, and vibrational motions are distinguished. Of particular importance, the vibrational degree of freedom enables the molecule to capture antiprotons having lab energies above 100 eV, whereas atomic capture cuts off sharply above the ionization threshold of 27 eV (in the lab system). Antiproton capture by the atom is calculated by the same method as well as by the classical-trajectory Monte Carlo method, which is applicable only to the atom. The initial quantum numbers (assigned quasiclassically) of the $\overline{p}p$ formed are found to be shifted to significantly smaller values for the molecular target; the n distribution is also narrower for the molecular target as compared with the atomic target. [S1050-2947(97)05011-7]

PACS number(s): 36.10.−k, 34.10.+x, 25.43.+t, 03.65.Sq

I. INTRODUCTION

Antiprotonic atoms, in which an antiproton $\overline{p}$ is bound to a normal nucleus, have been of interest since the discovery of the antiproton in 1955. Modern experiments include cascade and spectroscopy, probes of nuclear structure, and nuclear absorption and annihilation [1], and, recently, the Barkas effect on stopping powers [2–6], and anomalously long-lived mixed $\overline{p}/e^-$ atoms [7–10]. The most studied, experimentally and theoretically, and fundamental of these atoms is antiprotonic hydrogen $\overline{p}p$. Already in this simplest case, there is an experimental-theoretical disconnect (which also applies to capture of other heavy negative particles like μ^-, π^-, and K^-). All the experiments have been done with a molecular H_2 target,[1] while the theoretical subject has been an atomic H target or frozen molecule.

To connect experiments with theory, the earliest work assumed that the H_2 target could be represented by *two* separate H atoms (Bragg's rule), but it became clear that such an approximation is unjustified when it was shown that capture occurs only after the negative particle is slowed to an energy comparable to the target ionization potential (IP). Then it was suggested that the IP was the controlling parameter and that the stopping of $\overline{p}$ (or μ^-, etc.) by H_2 would be about the same as *one* H atom since the IP's are similar (15.4 eV for H_2 vs 13.6 eV for H). Furthermore, it was speculated that the cross section for H_2 would be slightly *larger* than that for H at the higher collision energies since H_2 has two electrons, a higher IP, and a larger geometric size, but slightly *smaller* at low energies because the molecule cannot be adiabatically ionized.[2] A coupled-channel semiclassical approximation (CCSA) with an adiabatic basis [17], which took into account the anisotropy of the molecule but ignored vibration and rotation, seemed to corroborate this conclusion with a crossover point at ~9 eV (for μ^-).[3]

There have been few calculations of $\overline{p}$ capture, but there have been a number of calculations of μ^- capture by the H atom, which is expected to be qualitatively similar. These include quantum-mechanical [19,20], quasiclassical [21], and model [18] calculations, which yield results in quite good agreement. Even for the atomic target, completely quantum-mechanical calculations are difficult. Generally time-independent quantal methods are not suitable since $\mu^- + \mathrm{H}$ at small distances is embedded in an electronic continuum and capture occurs in high Rydberg states; thus it is necessary to include a large number of lower-lying and intermediate states. Time-dependent methods, with the wave function solved on a spatial grid, have been used successfully, and their recent development [22] might make them even more apropos. However, the molecular target is still more difficult since the collision involves particle rearrangement and the Hartree-Fock H_2 molecule does not dissociate correctly.

On the other hand, the classical-trajectory Monte Carlo (CTMC) method is quite easy to apply, and has been used

---

*Electronic address: cohen@lanl.gov

[1] Formation in corotating beams of antiprotons and negative ions via $\overline{p}+\mathrm{H}^-$ collisions has been proposed [11] and calculated [12–14], but the experiment has not been carried out.

[2] Adiabatic ionization [15] in $\overline{p}+\mathrm{H}$ collisions occurs when the $\overline{p}$-p distance becomes small enough that the dipole formed can no longer bind an electron [16]. In the case of $\overline{p}+H_2$, the electron can migrate to the opposite end of the diatomic molecule, to form a stable negative atomic ion, and adiabatic ionization does not occur.

[3] The CCSA method is a generalization of the diabatic-states model used earlier [18] for atomic capture.

1050-2947/97/56(5)/3583(14)/$10.00

with remarkable success for $\mu^- + \mathrm{H}$ [21] and $\bar{p} + \mathrm{H}$ [13] collisions. But the CTMC method is generally limited to one-electron target atoms since molecules or multielectron atoms are classically unstable with respect to dissociation or autoionization. The utility of the quasiclassical approach was extended by Kirschbaum and Wilets (KW) [23], who introduced physically motivated constraining potentials which stabilize all quasiclassical atoms and many molecules. For atoms the KW model displays a shell structure; the total energies are fairly accurate (between the Thomas-Fermi and Hartree-Fock theories) and the ionization potentials are of useful accuracy (aside from a few shell anomalies) [24]. These quasiclassical atoms have proved useful for calculating ion-atom collisions [25], stopping powers [26], and characteristics of long-lived $\alpha\bar{p}e^-$ states [27]. But the simple molecules H_2 and $\mathrm{H}_2{}^+$ are seriously overbound by the KW model (the dissociation energies are 4–6 times, respectively, the true values). One can observe that this overbinding is due to the *localization* of the electron(s) at high-symmetry positions, namely at the molecular midpoint of $\mathrm{H}_2{}^+$ or the bisecting plane of H_2.

For atoms, a necessary condition for stability is that the electrons are not allowed to collapse to the symmetry point, i.e., to the nucleus. The effective potential enforcing this condition is motivated by the Heisenberg uncertainty principle $rp \geqslant \hbar$, where r and p are the distance and momentum of an electron with respect to a nucleus. For the H atom, this condition is equivalent to the de Broglie description of the hydrogen atom [28]. In a similar way, the effective potential that brings about a shell structure is motivated by the Pauli exclusion principle, which, somewhat less rigorously, is mimicked by the condition $r_{ij}p_{ij} \geqslant \xi_P \hbar$, where r_{ij} and p_{ij} are the relative distance and momentum of two electrons having like spin, and ξ_P is a constant of order unity. These potentials are of the form $r^{-2}f(rp)$, where f is some monotonically decreasing function of its argument.[4] In the same spirit, in this paper we introduce a similar ansatz to exclude the electrons from their high-symmetry points in the $\mathrm{H}_2{}^+$ and H_2 molecules. A very satisfactory form of these potentials is found to be $R^{-2}f(rp)$, which differs only in the internuclear distance R, instead of r, being used in the prefactor. Here r and p are relative to the midpoint in the case of the homonuclear molecule. The details are discussed in Sec. II A.

This extension of the KW model with molecular constraints (termed KWC) is used for the $\bar{p} + \mathrm{H}_2$ collision. The five-body dynamics is solved by formulating Hamilton's equations of motion including the momentum-dependent potentials. To our knowledge, this is the first calculation to include the molecular rotational and vibrational-dissociative degrees of freedom during $\bar{p}$ capture. The results show that the previous conjecture that negative-particle capture is mainly controlled by the ionization threshold is too simplistic. The capture cross sections for the H_2 target are presented in Sec. III, along with the n and l quantum numbers of the $\bar{p}p$ atom formed.[5]

II. QUASICLASSICAL METHOD

A. Momentum-dependent potentials and the Hamiltonian

In the KW model [23], the effective Hamiltonian is written

$$K_{\mathrm{KW}} = H_0 + V_H + V_P \tag{1}$$

where

$$H_0 = T + V_{\mathrm{Coul}} \tag{2}$$

is the usual Hamiltonian containing the kinetic energy and Coulomb potentials, and V_H and V_P are effective potentials representing the quantum-mechanical effects of the Heisenberg uncertainty and Pauli exclusion principles, respectively. Each contribution to V_H or V_P is of the form $r^{-2}f(rp)$, where r and p are the relative distance and momentum of an electron with respect to a (oppositely charged) nucleus in the case of V_H, and are the relative distance and momentum between two electrons of the same spin in the case of V_P.

In the present model (KWC) we introduce two additional terms to improve the treatment of the $\mathrm{H}_2{}^+$ and H_2 molecules; the effective Hamiltonian becomes

$$H_{\mathrm{KWC}} = H_{\mathrm{KW}} + V_{m1} + V_{m2} \tag{3}$$

where V_{m1} is a one-electron operator and V_{m2} is a two-electron operator, of form similar to V_H and V_P except with prefactor R^{-2}, where R is the internuclear distance, instead of r^{-2}. Following KW, we use

$$f(rp;\xi) \equiv \frac{(\xi\hbar)^2}{4\alpha} \exp\left\{ \alpha \left[1 - \left(\frac{rp}{\xi\hbar} \right)^4 \right] \right\}, \tag{4}$$

where ξ is one of four parameters: ξ_H, ξ_P, ξ_{m1}, and ξ_{m2}, discussed below, and a constant α ($\equiv 4$) whose precise value is unimportant but affects the ξ values. Note that $f(rp;\xi) \rightarrow 0$ as $\xi \rightarrow 0$, thus going over to the purely classical treatment.

For later reference it is convenient to build up the Hamiltonian for $\bar{p} + \mathrm{H}_2$ collisions, starting with that for the H atom. We will use the following notation: subscripts a for the antiproton, b and c for protons, 1 and 2 for electrons, o for the midpoint of the molecule, or α, β for any pair of these; the relative distance

$$\mathbf{r}_{\alpha\beta} = \mathbf{r}_\beta - \mathbf{r}_\alpha ; \tag{5}$$

the relative momentum

$$\mathbf{p}_{\alpha\beta} = \frac{m_\alpha \mathbf{p}_\beta - m_\beta \mathbf{p}_\alpha}{m_\alpha + m_\beta} ; \tag{6}$$

$$s_i = \text{ spin of electron } i \text{ (up or down);} \tag{7}$$

---

[4] The exact analytic form of f seems not to be too important, but its argument and prefactor conjoin to satisfy a virial theorem [23,24]. We use the form of f suggested by KW [23].

[5] Atomic units (a.u.), defined by $e = m_e = \hbar = 1$, are used except where otherwise indicated. In terms of familiar units, atomic units are 0.5292×10^{-8} cm (distance a_0), 27.21 eV (energy), and 2.188×10^8 cm/s (velocity).

TABLE I. Coordinates and momenta of the minimum-energy molecular configuration with $\alpha=4.0$, $\xi_H=0.9428$, $\xi_{m1}=0.90$, and $\xi_{m2}=1.73$. The minimum-energy states are planar, and the positions and momenta are given here in the $x-z$ plane (in atomic units).

	H_2				H_2^+			
	x	z	p_x	p_z	x	z	p_x	p_z
First nucleus	0	0.6955	0	0	0	1.1614	0	0
Second nucleus	0	−0.6955	0	0	0	−1.1614	0	0
First electron	0.8714	0.3283	1.0331	0	0.6572	0.5095	1.0362	0
Second electron	−0.8714	−0.3283	−1.0331	0				

and the reduced mass

$$\mu_{\alpha\beta}=\frac{m_\alpha m_\beta}{m_\alpha+m_\beta}, \tag{8}$$

with

$$m_0=2m_p. \tag{9}$$

The Hamiltonian for the H atom (with proton b and electron 1) is[6]

$$H[\mathrm{H}]=\frac{1}{2m_p}p_b^2+\frac{1}{2m_e}p_1^2-\frac{e^2}{r_{b1}}+\frac{1}{\mu_{b1}r_{b1}^2}f(r_{b1}p_{b1};\xi_H). \tag{10}$$

It is from minimization of Eq. (10) that the value of ξ_H is fixed to give the correct binding energy of the H atom. The resulting minimum for the H atom occurs at $r=1.0$ and $p=0.9428$. With the addition of a second proton (c) to make H_2^+,

$$H[\mathrm{H}_2^+]=H[\mathrm{H}]+\frac{1}{2m_p}p_c^2+\frac{e^2}{r_{bc}}-\frac{e^2}{r_{c1}}+\frac{1}{\mu_{c1}r_{c1}^2}f(r_{c1}p_{c1};\xi_H)+\frac{1}{\mu_{o1}r_{bc}^2}f(r_{o1}p_{o1};\xi_{m1}). \tag{11}$$

The value of ξ_{m1} is fixed such that the minimum of Eq. (11) is the correct energy of the H_2^+ molecular ion. Then, for H_2,

$$\begin{aligned}H[\mathrm{H}_2]=H[\mathrm{H}_2^+]&+\frac{1}{2m_e}p_2^2-\frac{e^2}{r_{b2}}-\frac{e^2}{r_{c2}}+\frac{e^2}{r_{12}}\\&+\frac{1}{\mu_{b2}r_{b2}^2}f(r_{b2}p_{b2};\xi_H)+\frac{1}{\mu_{c2}r_{c2}^2}f(r_{c2}p_{c2};\xi_H)\\&+\frac{1}{\mu_{12}r_{12}^2}f(r_{12}p_{12};\xi_P)\,\delta_{s_1,s_2}\\&+\frac{1}{\mu_{o2}r_{bc}^2}f(r_{o2}p_{o2};\xi_{m1})+\frac{1}{\mu_{12}r_{bc}^2}f(r_{12}p_{12};\xi_{m2}).\end{aligned} \tag{12}$$

In the present work, the H_2 target is taken to be in its (singlet) ground state, and spin-orbit coupling is neglected, so the term in ξ_P vanishes (this term would be positive definite for like spins). Then the value of ξ_{m2} is fixed such that the minimum of Eq. (12) is the correct energy of the H_2 molecule.

Finally the complete Hamiltonian for the $\overline{p}+H_2$ collision is given by

$$\begin{aligned}H[\overline{p}+\mathrm{H}_2]=H[\mathrm{H}_2]&+\frac{1}{2m_p}p_a^2-\frac{e^2}{r_{ba}}-\frac{e^2}{r_{ca}}+\frac{e^2}{r_{a1}}+\frac{e^2}{r_{a2}}\\&+\frac{1}{\mu_{ba}r_{ba}^2}f(r_{ba}p_{ba};\xi_H)+\frac{1}{\mu_{ca}r_{ca}^2}f(r_{ca}p_{ca};\xi_H)\\&+\frac{1}{\mu_{oa}r_{bc}^2}f(r_{oa}p_{oa};\xi_{m1}).\end{aligned} \tag{13}$$

Note that there are no new parameters in this last expression.

For comparison purposes, we will also do calculations on $\overline{p}+H$ collisions, with the Hamiltonian

$$H[\overline{p}+\mathrm{H}]=H[\mathrm{H}]+\frac{1}{2m_p}p_a^2-\frac{e^2}{r_{ba}}+\frac{e^2}{r_{a1}}+\frac{1}{\mu_{ba}r_{ba}^2}f(r_{ba}p_{ba};\xi_H). \tag{14}$$

Note that the CTMC Hamiltonian is obtained in the limit $\xi_H\rightarrow 0$.

B. Ground-state and clamped-nuclei energies

At the minima of the KW and KWC functionals, the values of all particle (electrons and nuclei) positions **r** and momenta **p** are fixed to within *independent* rigid-body rotations when the molecular center of mass is fixed at the origin. This energy depends on the parameters ξ_H, ξ_{m1}, and ξ_{m2}, which are determined as follows: $\xi_H=0.9428$ to give the H-atom ground-state energy (−0.5 a.u.), *then* $\xi_{m1}=0.90$ to give the ground-state energy of H_2^+ (−0.603 a.u.), *then* $\xi_{m2}=1.73$ to give the ground-state energy of H_2 (−1.174 a.u.). The coordinates and momenta for the ground-state configurations are given in Table I. The model is now completely defined, for collisions as well as for molecular structure.

One of the great advantages of the quasiclassical method is the ease of treating nonadiabatic behavior, i.e., the coupling of nuclear and electronic motions. However, it is still instructive to view the Born-Oppenheimer-like energies, both because of the availability of accurate quantum-

---

[6] The conventional notation here uses H for "Hamiltonian," "hydrogen," and "Heisenberg." The context should make the meaning clear.

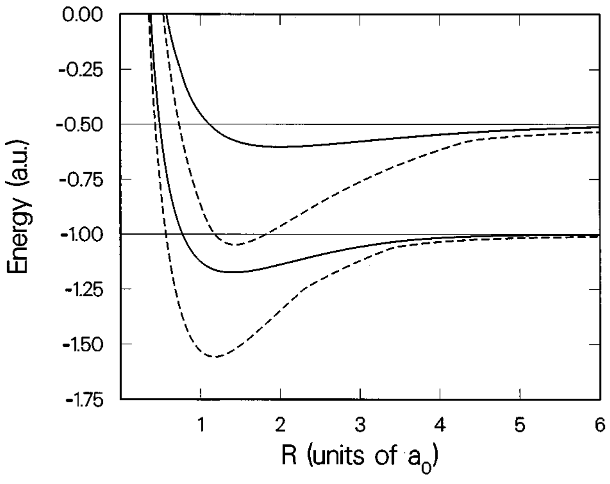

FIG. 1. Unmodified KW (dashed curve) and quantum-mechanical (full curve) potential curves for H_2 (lower pair) and H_2^+ (upper pair). Note overbinding in the KW model.

mechanical Born-Oppenheimer potential curves and the importance of Franck-Condon-like (vertical or fixed R) electronic transitions. For ionizing and/or dissociative transitions, the relative positions of the minimum of the lower curve and the sigma point (where the attractive potential curve crosses the asymptotic energy value) of the upper curve can be especially important. The quasiclassical potential curves are obtained by conditionally minimizing Eq. (12) with $r_{bc} \equiv R$ fixed, as a function of parameter R.

The potential curves of the unmodified KW treatment (obtained in the limit ξ_{1m} and $\xi_{2m} \to 0$) for H_2 and H_2^+ are shown in Fig. 1. Both are greatly overbound. The reason can be inferred from the KW columns of Fig. 2, which shows the positions of the electron(s) at the minima. The classical electrons occupy the symmetry points where the screening of the *p*-*p* Coulomb repulsion is maximized. Quantum mechanically, of course, an atomic or molecular electron cannot be localized at a point, and the screening is reduced. Within a classical dynamics approach, it is still highly desirable to deal with point particles, but it is possible to effectively spread them out by repelling them from the symmetry point. This is accomplished by the potentials V_{1m} and V_{2m}. The Hamiltonian maintains the axial symmetry of the diatomic molecule, but the ground-state configuration spontaneously breaks this symmetry as shown in the KWC columns of Fig. 2. In effect, the one-dimensional (1D) coalescence becomes a 2D surface. The resulting potential curves are shown in Fig. 3. They are in excellent agreement with the quantum-mechanical curves in the range relevant to the present application.

For completeness, though it is of little consequence in the present work, we note that at *large* distances the KWC induced dipole moments are zero order,[7] as can be seen in Fig. 2, rather than the correct first order, and the potential curves thus become too attractive. Of course, in real collisions the electron is not fixed, even classically, and the motion will tend to wash out the zero-order contribution. At very *small R* the KWC potential curves behave correctly as R^{-1}. The energy difference at $R = 0.01\ a_0$, near the united-atom limit, is about 18 eV, which can be compared with the true ionization potential of 24.6 eV for the He atom. The electronic binding energy in the H_2 united-atom limit is smaller than that of the KW He atom, where the ionization potential is 28.9 eV, because of the extra constraining potentials (including double counting of V_H).

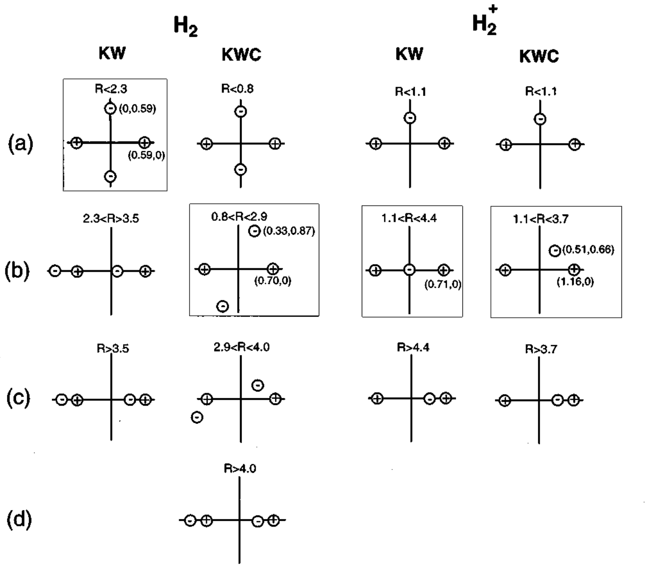

FIG. 2. Minimum-energy configurations for H_2 and H_2^+ in the KW and KWC models for different ranges of fixed internuclear distance R. Protons are designated by + signs and electrons by − signs. All topologically distinguishable configurations are shown. Boxes are drawn around the configuration in the range containing the minimum of the potential curve, and the positions of the particles at the global minimum are indicated.

C. Trajectories and cross sections

The calculation of each trajectory proceeds in three steps: (i) choose initial conditions (r_0 and p_0 for all particles), (ii)

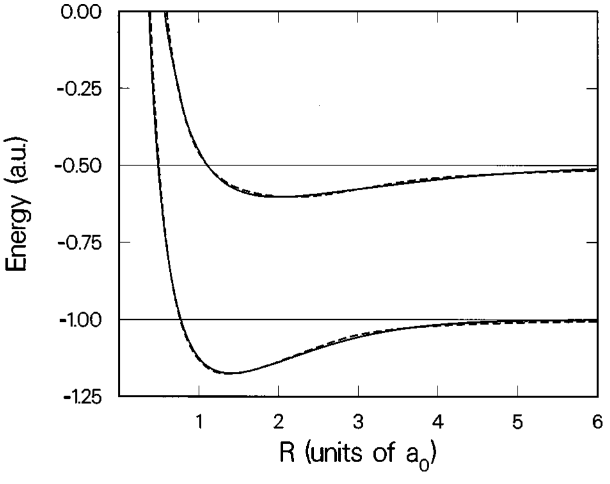

FIG. 3. KWC (dashed curve) and quantum-mechanical (full curve) potential curves for H_2 (lower pair) and H_2^+ (upper pair).

---

[7] Zero order means that an arbitrarily small electric field can induce the maximum dipole moment in the static limit. In first order, the dipole moment is proportional to the field.

integrate Hamilton's classical equations of motion, and (iii) examine asymptotic trajectory for final state. The equations are solved in a space-fixed system, unlike our previous work [21,13], where barycentric coordinate systems were employed. For more than four bodies the disadvantage due to the complexity of the equations in barycentric coordinates outweighs the advantage of eliminating the equations for the center-of-mass motion. The target H_2 is initially placed at the origin with the coordinates and momenta given in Table I, and independent random Euler rotations are applied to each. The projectile is started at $x=-10\,a_0$ with impact parameter b chosen by uniform sampling of $b^2\in[(b_{i-1})^2,(b_i)^2]$. In the first range $[b_0,b_1]$, $b_0=0$ and b_1 is taken to be such that a few (typically 3–4) ranges of impact parameters will be required to converge the cross sections with $b_{i+1}=\sqrt{2}b_i$.

The present space-fixed code was verified by comparison with the previous, mostly independent, barycentric code for a variety of three- and four-body calculations.

The computer code is capable of recognizing all particle rearrangements, including those containing both $\bar{p}$ and e^-. However, such combined $\bar{p}\text{-}e^-$ atoms are generally short lived. Metastable states of $\alpha\bar{p}e^-$ exist, but analogous states like $p\bar{p}e^-$ or $pp\bar{p}e^-$ are not known. More relevant is the state of $p\bar{p}$ *after* the electron has been ionized. In almost all cases it was possible to run the trajectory long enough to determine a definite state of $p\bar{p}$.

After accumulation of the results of the trajectories, the cross section for a reaction R is given by

$$\sigma_R=\sum_i \sigma_R^{(i)} \tag{15}$$

in terms of the partial cross sections

$$\sigma_R^{(i)}=\frac{N_i^{(R)}}{N_i^{\mathrm{tot}}}\pi[(b_i)^2-(b_{i-1})^2], \tag{16}$$

where $N_i^{(R)}$ is the number of trajectories in which R occurred out of the total N_i^{tot} trajectories run with $b\in[b_{i-1},b_i]$. In the limit $N_i^{\mathrm{tot}}\to\infty$, the *ratio* $N_i^{(R)}/N_i^{\mathrm{tot}}$ becomes constant. The standard statistical error in σ_R is

$$\Delta\sigma_R=\left(\sum_i (\Delta\sigma_R^{(i)})^2\right)^{1/2} \tag{17}$$

in terms of the error in each interval,

$$\Delta\sigma_R^{(i)}=\sigma_R^{(i)}\left(\frac{N_i^{\mathrm{tot}}-N_i^{(R)}}{N_i^{\mathrm{tot}}N_i^{(R)}}\right)^{1/2}. \tag{18}$$

For $\bar{p}+H_2$ calculations, 100 trajectories were run in each range of impact parameters with $b_1=1.5a_0$, except at the smallest collision energies ($b_1=3.0a_0$ was used for $E_{\mathrm{c.m.}}=0.1$ a.u. and $b_1=5.0a_0$ for $E_{\mathrm{c.m.}}=0.01$ a.u.). For $\bar{p}+\mathrm{H}$ calculations, ten times as many trajectories were run.

III. RESULTS

The main focus of this work is on $p\bar{p}$ formation in collisions of $\bar{p}$ with the H_2 molecule. Features that do not occur in atomic capture are of particular interest. The KWC method fully treats all the molecular degrees of freedom. We attempted to isolate the molecular effects by test calculations at three levels: (i) by using the same method to do $\bar{p}+\mathrm{H}$ collisions, for which there are no molecular effects, (ii) by using the same method to do $\bar{p}+H_2$ with the diatomic target constrained as a rigid rotor (i.e., with the $p\text{-}p$ distance fixed, but no other degrees of freedom restricted), and (iii) by using the same method treating H_2 as a rigid ''nonrotor'' (i.e., with the $p\text{-}p$ vector having fixed magnitude *and* spatial orientation). The $\bar{p}+\mathrm{H}$ calculations interest us for another reason; they can be done with the standard CTMC method as well as the KW method. Results of these two methods will now be compared.

A. $\bar{p}+\mathrm{H}$: CTMC and KW calculations

Cross sections for $p\bar{p}$ formation in low-energy collisions of $\bar{p}$ with the hydrogen atom have previously been calculated using the CTMC method [13]. That work showed that the $\bar{p}+\mathrm{H}$ capture cross section is quite similar to the $\mu^-+\mathrm{H}$ capture cross section. Both are monotonically decreasing as a function of collision energy with a sharp decrease at a c.m. collision energy of 0.5 a.u., which is the IP of the target atom. Above 0.5 a.u. the ionized electron must carry off the excess as kinetic energy. The two reactions differ significantly only in this region, where the $\bar{p}+\mathrm{H}$ capture cross section falls off even more rapidly than that of $\mu^-+\mathrm{H}$, corresponding to the more adiabatic behavior of the reaction with the heavier particle [13].

The CTMC and KW results for the $p\bar{p}$ formation are given in Tables II and III, respectively, and shown in Fig. 4 along with the corresponding total ionization cross sections. The CTMC results are the same as in Ref. [13] except that more trajectories were run, and consequently the error bars are smaller. The agreement between the two methods is satisfactory. The KW cross section is somewhat higher at the lowest collision energies and somewhat lower at higher energies. It is interesting to note that, in the case of $\mu^-+\mathrm{H}$ collisions,[8] a similar small difference was found between the classical-quantal-coupling method [20] and the CTMC method. More applications will be required to tell whether KW really is a significant improvement in the quasiclassical treatment of the one-electron case.

The distribution of quantum numbers n,l for the initially formed $p\bar{p}$ atom is the next important characteristic. It provides the initial conditions for the subsequent cascade, which also depends on the target density and temperature as well as any admixture of other species. The initial-state distribution is actually a product of the competition between slowing down,

$$\bar{p}+\mathrm{H}\to\begin{cases}\bar{p}+\mathrm{H}^++e^-\\ \bar{p}+\mathrm{H}^*\end{cases}, \tag{19}$$

and capture,

$$\bar{p}+\mathrm{H}\to p\bar{p}(n,l)+e^-, \tag{20}$$

---

[8] For comparison of several methods used for μ^- capture by the H atom, see Ref. [29].

TABLE II. Cross sections ($\sigma_{\bar{p}p}$ and σ_{tot}), parameters for fits of n distributions (n_0 and γ—see Appendix A), and parameters for fits of l distributions (b, a, and l_1—see Appendix B) for $\bar{p}p$ atoms formed in $\bar{p}+\text{H}$ collisions, calculated by the CTMC method.

$E_{\text{c.m.}}$ (a.u.)	$\sigma_{\bar{p}p}$ (a_0^2)	σ_{tot} (a_0^2)	n_0	γ	b	a	l_1
0.01	67.41±2.10	67.41±2.11	29.55	0.91	-3.25×10^{-2}	1.31×10^{-3}	30
0.10	15.91±0.44	15.91±0.44	32.53	1.18	-5.39×10^{-3}	2.03×10^{-3}	34
0.20	11.42±0.12	11.42±0.12	37.12	1.53	2.96×10^{-3}	3.66×10^{-3}	39
0.30	9.97±0.12	9.97±0.12	44.40	2.74	-3.11×10^{-3}	8.22×10^{-3}	47
0.40	8.99±0.13	8.99±0.13	57.94	6.31	-1.87×10^{-3}	5.91×10^{-2}	60
0.50	8.25±0.14	8.25±0.14	97.49	25.23	-2.27×10^{-4}	1.69×10^{-1}	74
0.55	3.21±0.12	8.12±0.20	112.28	41.26	1.03×10^{-2}	5.11×10^{-1}	76
0.60	0.58±0.06	8.01±0.16	108.20	70.11	7.27×10^{-2}	$5.04\times10^{+0}$	78
0.70	0.06±0.02	7.73±0.14	[a]				
0.80	0.01±0.01	7.41±0.15					
1.00	≲0.004	7.13±0.15					

[a] There were not enough trajectories forming $\bar{p}p$ at the higher energies to allow reliable fits of the quantum-number distributions.

since it depends on the collision energy. For example, the n quantum-number histograms and the fits (see Appendix A) are shown in Fig. 5 for two different collision energies. A rigorous formulation of the capture distributions has been given in terms of the "arrival function" $F_{\text{arr}}(E)$, which is a solution of an integral equation involving the energy-dependent differential energy-loss cross section [30,21]. In principle, this differential cross section is required at all energies, ranging from that of the fast (≥1 keV) free antiproton down to near zero since some antiprotons are not captured until they are essentially stationary.

In the present work, cross sections have not been calculated at energies higher than where capture is probable. Even so, an observation made in Ref. [21] allows the initial distribution to be calculated approximately. That is, it was observed that the mechanisms of reactions (19) and (20) were similar, with capture resulting when the energy loss (target IP plus kinetic energy of the ionized electron) exceeds the incident energy of the $\bar{p}$. Hence the typical energy loss in slowing down is comparable to the collision energy where capture occurs. As long as the typical energy loss is comparable to or greater than the energies at which capture occurs, the arrival function $F_{\text{arr}}(E)$ is fairly flat and the capture profile

$$F_{\text{capt}}(E)=\frac{\sigma_{\text{capt}}(E)}{\sigma_{\text{tot}}(E)}F_{\text{arr}}(E) \qquad (21)$$

is adequately determined by just the ratio of cross sections to within a normalization constant.

Thus we make the approximation

$$P_n=\int F_n(E)F_{\text{capt}}(E)dE\approx N_n\int F_n(E)\frac{\sigma_{\text{capt}}(E)}{\sigma_{\text{tot}}(E)}dE, \qquad (22)$$

where N_n is a normalization constant. We also neglect the contributions of elastic and nonionizing inelastic scattering to slowing down, so σ_{tot} is approximated by the total ionization cross section.

Direct calculations of $F_n(E)$, $\sigma_{\text{capt}}(E)$, and $\sigma_{\text{tot}}(E)$ are made at only a few energies (those in Tables II and III). In carrying out the quadrature of Eq. (22), spurious structures can result if $F_n(E)$ is not accurately interpolated, and the quadrature performed with a fairly small energy step. We found a satisfactory spline interpolation scheme (see Appendix A) that depends mainly on the peak n_0 and width γ of the distribution F_n at each calculated energy. Their values are given in Tables II and III. This procedure smoothes the statistical histogram as well as providing adequate, physically

TABLE III. Cross sections ($\sigma_{\bar{p}p}$ and σ_{tot}), parameters for fits of n distributions (n_0 and γ—see Appendix A), and parameters for fits of l distributions (b, a, and l_1—see Appendix B) for $\bar{p}p$ atoms formed in $\bar{p}+\text{H}$ collisions, calculated by the KW method.

$E_{\text{c.m.}}$ (a.u.)	$\sigma_{\bar{p}p}$ (a_0^2)	σ_{tot} (a_0^2)	n_0	γ	b	a	l_1
0.01	163.21±5.06	166.19±5.19	29.45	0.93	-2.90×10^{-2}	1.81×10^{-3}	31
0.10	19.00±0.42	19.00±0.42	32.31	1.24	6.14×10^{-3}	2.31×10^{-3}	34
0.20	10.64±0.12	10.64±0.12	36.66	1.76	1.31×10^{-2}	1.15×10^{-2}	38
0.30	8.04±0.10	8.04±0.10	43.53	2.94	1.57×10^{-2}	2.47×10^{-2}	42
0.40	6.56±0.10	6.56±0.10	56.14	6.80	1.08×10^{-2}	1.83×10^{-2}	44
0.50	5.51±0.10	5.61±0.10	88.67	16.67	3.73×10^{-2}	2.79×10^{-1}	56
0.55	2.56±0.11	5.25±0.15	132.55	52.82	3.68×10^{-2}	5.86×10^{-1}	58
0.60	0.21±0.04	5.08±0.11	178.08	192.89	1.11×10^{-1}	$2.45\times10^{+0}$	60
0.70	0.01±0.01	4.54±0.11					
0.80	≲0.004	4.35±0.11					

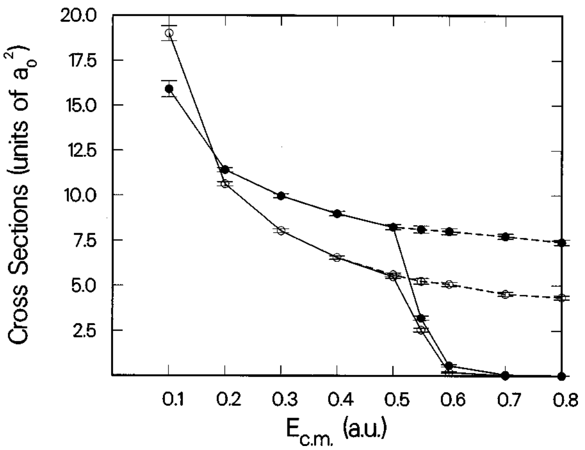

FIG. 4. Capture (full curve) and total ionization (dashed curve) cross sections for $\bar{p}+\mathrm{H}$ calculated by the KW (open circles) and CTMC (closed circles) methods. At collision energies below the target ionization threshold, ionization can occur only if the $\bar{p}$ is captured.

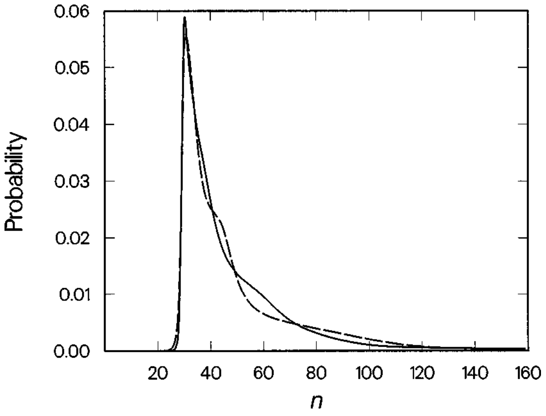

FIG. 6. Distribution of n quantum numbers of $\bar{p}p$ resulting from $\bar{p}$ capture by atomic H, integrated over collision energies using the KW results (full curve) and the CTMC results (dashed curve).

motivated fits. The integrated distributions, calculated in the CTMC and KW models, are shown in Fig. 6. They are in good agreement.

The distributions of l, summed over n, and their fits (see Appendix B) at a midrange capture energy, are shown in Fig. 7. The corresponding distributions, integrated over capture energy, are shown in Fig. 8. They are similar except that the CTMC-calculated distribution extends to higher values of l. An interpretation given in Ref. [21] suffices to explain this difference. It was shown there (for μ^- capture) that the main features of the l distribution are qualitatively interpretable in terms of the overlap of the unperturbed orbital of the target electron with the orbital of the captured heavy negative par-

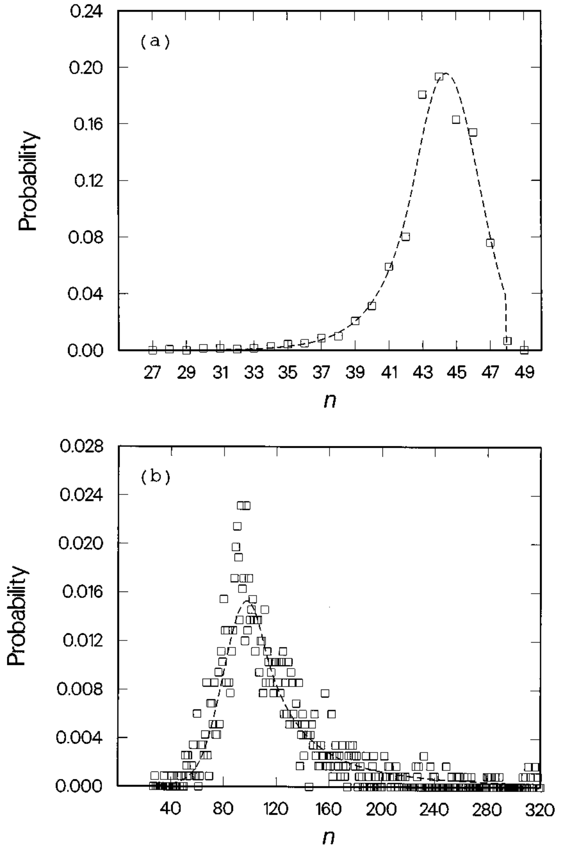

FIG. 5. Distribution of n quantum numbers of $\bar{p}p$ resulting from $\bar{p}$ capture by the H atom, calculated by the CTMC method at energies (a) $E_{\mathrm{c.m.}}=0.30$ a.u. and (b) $E_{\mathrm{c.m.}}=0.50$ a.u. The points are the results of the Monte Carlo trajectories ($\sim$1300 contributing to each case), and the dashed curve is a fit (see Appendix A).

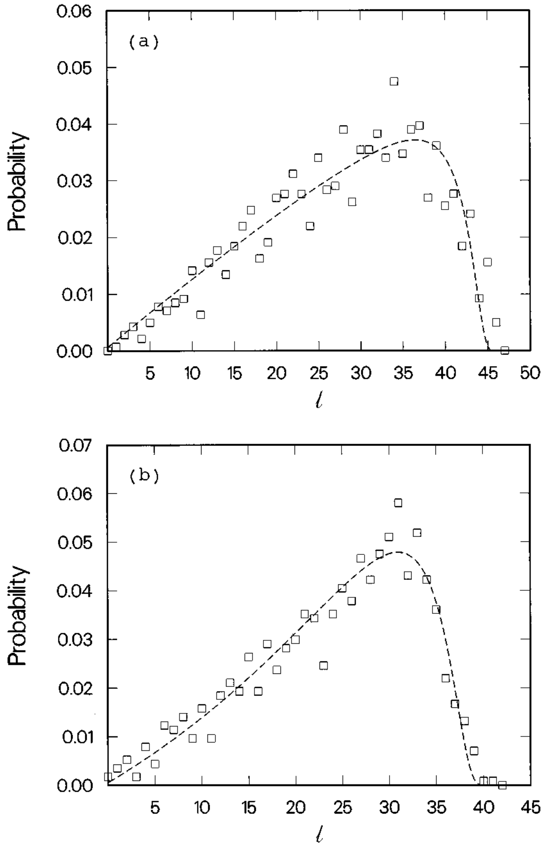

FIG. 7. Distribution of l quantum numbers for $\bar{p}$ capture by the H atom at a collision energy $E_{\mathrm{c.m.}}=0.30$ a.u., calculated by the (a) CTMC and (b) KW methods. The points are the results of the Monte Carlo trajectories ($\sim$1300 contributing to each case), and the dashed curve is a fit (see Appendix B).

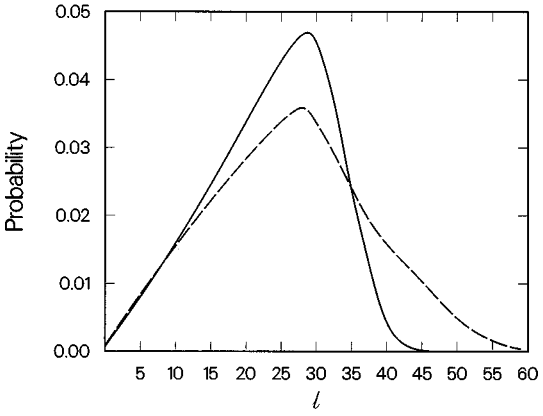

FIG. 8. Distribution of l quantum numbers of $\bar{p}p$ resulting from $\bar{p}$ capture by atomic H, integrated over collision energies using the KW results (full curve) and the CTMC results (dashed curve).

ticle (of reduced mass μ in units of m_e) for large n ($\gtrsim\sqrt{2\mu}$). Based on this simple consideration, the *maximum l* populated in CTMC calculations is

$$l_{\text{max}}^{\text{CTMC}}\approx 2\sqrt{\mu}\left(1-\frac{\mu}{n^2}\right)^{1/2} \tag{23}$$

corresponding to zero-angular-momentum electrons (eccentricity 1.0 with classical turning point at $2.0a_0$), and the *peak* in the l distribution occurs at

$$l_{\text{peak}}^{\text{CTMC}}\approx \sqrt{2\mu}\left(1-\frac{\mu}{2n^2}\right)^{1/2} \tag{24}$$

corresponding to maximum angular-momentum ($l=1.0$) electrons (eccentricity 0 with classical distance 1.0 a_0). Capture orbitals near $l_{\text{max}}^{\text{CTMC}}$ overlap only with the most eccentric electron orbitals in the microcanonical distribution, while those below $l_{\text{peak}}^{\text{CTMC}}$ overlap with all the target electron orbitals. It can be seen in Fig. 8 (dashed curve) that this is a faithful representation; for $\bar{p}p$, $l_{\text{max}}^{\text{CTMC}}(\text{all } n)=61$. The agreement with formula (24) for the peak cannot be ascertained from Fig. 8 since the distribution has been summed over n. For this purpose it is necessary to look at capture in a specific n state, where our Monte Carlo statistics are not as good. As an example, CTMC results, along with a nonlinear least-squares fit (see Appendix B), are shown for $n=57$ in Fig. 9(a); the values $l_{\text{max}}^{\text{CTMC}}(57)\approx 51$ and $l_{\text{peak}}^{\text{CTMC}}(57)\approx 40$ from Eqs. (23) and (24) are close to the fit.

In the KW model, *all* initial electron orbits have distance 1.0 a_0 from the nucleus. The same considerations then yield

$$l_{\text{max}}^{\text{KW}}\approx l_{\text{peak}}^{\text{KW}}\approx \sqrt{2\mu}\left(1-\frac{\mu}{2n^2}\right)^{1/2}. \tag{25}$$

The value $l_{\text{max}}^{\text{KW}}(\text{all } n)\approx 43$ is borne out by Fig. 8 (full curve). The peak in this figure occurs at a somewhat lower value value because some $\bar{p}p$'s are formed in lower n states and, of course, l must be less than n. Figure 9(b) shows that the distribution found for $n=57$ is in good agreement with the values $l_{\text{max}}^{\text{KW}}\approx l_{\text{peak}}^{\text{KW}}\approx 40$ predicted by Eq. (25). It should be emphasized that the estimates of Eqs. (23)–(25) are provided for heuristic purposes, and in no sense are rigorous bounds.

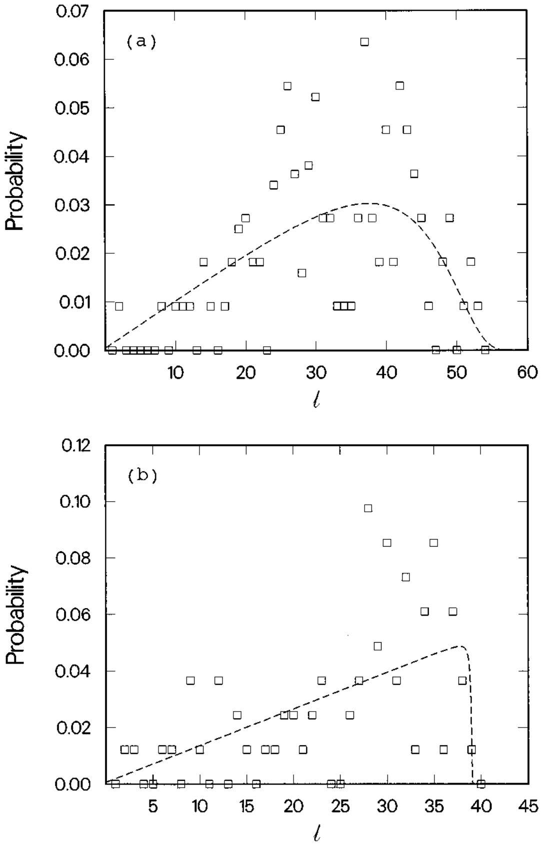

FIG. 9. Distribution of l quantum numbers, integrated over collision energies, for $\bar{p}$ capture by atomic H to form a $\bar{p}p$ atom having $n=57$, calculated using the (a) CTMC and (b) KW methods. The points are the results of the Monte Carlo trajectories (~100 contributing to each case), and the dashed curve is a fit (see Appendix B).

B. $\bar{p}+H_2$: KWC calculations

In capture of $\bar{p}$ by H_2, intermediate states such as $pp\bar{p}e^-$ or $p\bar{p}e^-$ are possible, but are predissociative and/or autoionizing. For this reason we have adopted the approach of following the trajectories long enough that the isolated $\bar{p}p$ atom can be characterized. The reactions distinguished are then

$$\bar{p}+H_2\rightarrow\begin{cases}\bar{p}p+H+e^- & \text{(26a)}\\ \bar{p}p+H^- & \text{(26b)}\\ \bar{p}p+p+e^-+e^-. & \text{(26c)}\end{cases}$$

The total capture cross sections $\sigma_{\bar{p}p}$ are given in Table IV and shown in Fig. 10. Additionally, the total reactive cross sections σ_{tot} (including dissociation and ionization as well as capture) are given in Table IV.

The mechanism seen in most $\bar{p}+H_2$ reactive collisions is that one electron is ionized upon close approach of the $\bar{p}$, leaving behind an unstable $pp\bar{p}e^-$ complex. At the higher energies the ionization is usually prompt, but at the lower energies a five-body precursor complex often survives for several vibrational periods (occasionally even splitting into $p\bar{p}e^-+H$ before ionization). The $pp\bar{p}e^-$ complex then usually dissociates into $\bar{p}p+H$ after the first electron is far removed. In fact, the reaction products are so strongly domi-

TABLE IV. Cross sections ($\sigma_{\bar{p}p}$ and σ_{tot}), parameters for fits of n distributions (n_0 and γ—see Appendix A), and parameters for fits of l distributions (b, a, and l_1—see Appendix B) for $\bar{p}p$ atoms formed in $\bar{p}+\text{H}_2$ collisions, calculated by the KWC method.

$E_{\text{c.m.}}$ (a.u.)	$\sigma_{\bar{p}p}$ (a_0^2)	σ_{tot} (a_0^2)	n_0	γ	b	a	l_1
0.01	148.32 ± 10.97	148.32 ± 10.97	24.58	1.32	-7.38×10^{-3}	6.88×10^{-4}	21
0.10	43.42 ± 1.67	43.42 ± 1.67	25.15	1.56	-8.85×10^{-4}	1.02×10^{-2}	27
0.20	28.11 ± 0.89	28.40 ± 0.90	25.72	3.51	-4.00×10^{-3}	2.35×10^{-4}	30
0.40	15.61 ± 0.57	20.14 ± 0.88	26.20	3.71	-2.61×10^{-3}	1.67×10^{-3}	32
0.60	11.03 ± 0.38	17.25 ± 0.80	27.07	4.54	-1.90×10^{-3}	3.91×10^{-2}	50
0.80	7.98 ± 0.40	15.83 ± 0.84	25.88	2.05	-8.30×10^{-4}	9.05×10^{-2}	52
1.00	6.28 ± 0.37	14.07 ± 0.73	26.41	1.81	-4.88×10^{-4}	1.37×10^{-1}	55
1.20	4.38 ± 0.36	12.58 ± 0.76	27.92	4.42	2.90×10^{-3}	$1.65\times10^{+0}$	57
1.60	2.12 ± 0.33	11.73 ± 0.73	31.29	8.57	3.94×10^{-3}	$2.29\times10^{+0}$	59
2.00	1.34 ± 0.28	11.03 ± 0.70					
2.40	0.85 ± 0.23	10.74 ± 0.71					
2.80	0.28 ± 0.14	9.97 ± 0.64					
4.00	0.07 ± 0.07	9.47 ± 0.67					
6.00	$\lesssim0.04$	8.91 ± 0.68					

nated by Eq. (26a) that quantitative presentation of cross sections for Eqs. (26b) and (26c) is not statistically justified. Qualitatively speaking, Eq. (26b) was seen in up to ~2% of the trajectories at the lowest energies, though it should be noted that H^- is overbound in the KW model (by 0.063 a.u. as compared to the experimental value of 0.028 a.u.). Reaction (26c) was seen even more rarely, $\lesssim1\%$ of the time at collision energies below 1 a.u., though it appears to become relatively more common at higher energies (where the total $\bar{p}p$ formation cross section is small).

Figure 10 shows that the $\bar{p}$ capture cross section for H_2 is more than a factor of 2 larger than that of H at all collision energies except the very lowest (0.01 a.u.).[9] More important, the $\bar{p}p$ formation with the molecular target extends to much higher collision energies. There are three notable possible sources of this difference: (i) the two-center, two-electron structure of H_2 (even though the first ionization potentials are similar); (ii) molecular vibrations and dissociation, and (iii) molecular rotations. Note that a dissociative result is not, by itself, proof that the dissociative coordinate was important for the $\bar{p}$ capture since, in principle, predissociation could occur after a purely electronic excitation. In fact, dissociation *must* eventually occur in the present calculations if the excitation energy exceeds the dissociation energy since we do not take radiative relaxation into account. If the dissociation dynamics occurred only after the collision (i.e., after the $\bar{p}p$ was far removed), then it would not affect the capture cross section.

In order to distinguish rotational effects from vibrational-dissociative effects, we performed the calculation treating the H_2 target as a rigid rotor—with the internuclear distance fixed at $R=R_0=1.4\ a_0$ but otherwise unhindered. This constraint is imposed by addition of a Lagrange multiplier term to the Hamiltonian (see Appendix C). This special calculation may also prove useful for comparing with future quantum-mechanical calculations. Quantum mechanically, the rigid-rotor approximation is a great simplification. Quasiclassically the treatment provides insight but the effort required for solution of the equation of motion is basically unchanged.

The $\bar{p}$ capture cross section in the rigid-rotor approximation is also shown in Fig. 10. It lies in between the results for the H atom and vibrating H_2 molecule at all energies. However, it is close to the H_2 result at collision energies below ~0.8 a.u. and falls to zero much more rapidly than does the cross section for the unconstrained target. As might be expected, it appears that only rotational excitation is probable at low impact energies while vibrational excitation becomes probable at the higher energies. The dividing energy is close

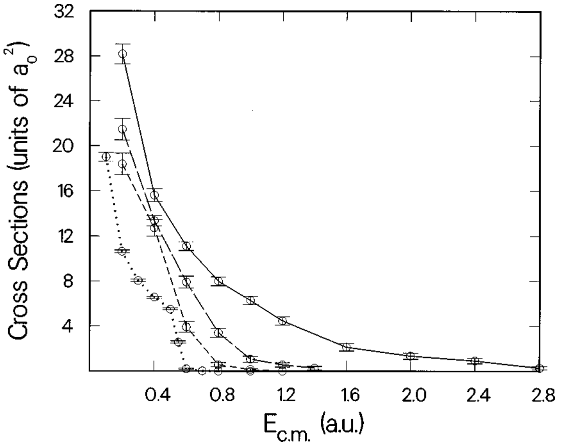

FIG. 10. Cross sections for $\bar{p}p$ formation in collisions of $\bar{p}p$ with the H_2 molecule (full curve). This calculation was done with the quasiclassical KWC method including full five-body dynamics. The other curves, shown for comparison, use the same method treating H_2 as a rigid rotor (long-dashed curve), treating H_2 as a rigid nonrotor (short-dashed curve), and for the H-atom target (dotted curve). The circles show the calculated points, which are connected by straight-line segments. Note that the laboratory-frame energy, E_{lab}, is $1.5E_{\text{c.m.}}$ for $\bar{p}+\text{H}_2$ and $2.0E_{\text{c.m.}}$ for $\bar{p}+\text{H}$.

---

[9] The calculations at $E=0.01$ a.u. were done primarily to obtain the n,l distributions. The cross sections are not necessarily accurate or converged, since the starting distance of $10a_0$ is not really far enough for such a slow collision.

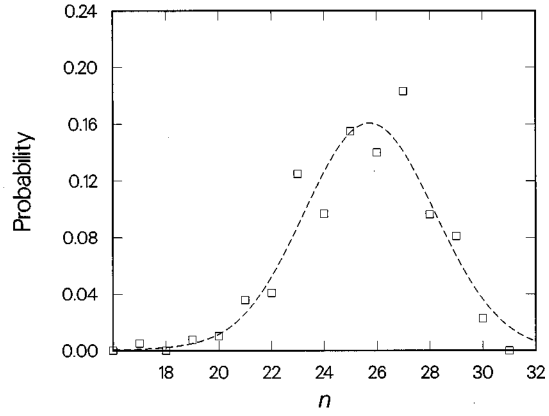

FIG. 11. Distribution of n quantum numbers of $p\bar{p}$ resulting from $\bar{p}$ capture by the H_2 molecule, calculated by the KWC method at energy $E_{\mathrm{c.m.}}=0.20$ a.u. The points are the results of the Monte Carlo trajectories ($\sim$300 contributing), and the dashed curve is a fit (see Appendix A).

to the energy ($E_{\mathrm{c.m.}}\approx1.0$ a.u.) where the cross sections peak for vibrational excitation of H_2 by H^+ impact [31]. At energies above 2.0 a.u. the $\bar{p}$ capture cross section essentially vanishes when vibration is disabled. With the vibrational degree of freedom enabled, it extends to much higher energies and falls off in a manner similar to the $H^+ + H_2$ vibrational excitation cross section [31].

In order to further investigate the effect of internal molecular dynamics, we also did rigid- ''nonrotor'' calculations in which the target was constrained not to rotate or vibrate (see Appendix D). As can be seen in Fig. 10, the $\bar{p}$ capture cross section then falls off even more rapidly then in the rigid-rotor case. As in the atomic case, the rigid-nonrotor capture cross section rapidly decreases above the ionization potential, which is 0.605 a.u. for R fixed at $1.4a_0$. However, the rigid-nonrotor cross section is still substantially larger than the atomic cross section, showing that the two-center, two-electron effect is also important.

The n and l distributions of $p\bar{p}$ formed in $\bar{p}+H_2$ collisions also differ significantly from those calculated for $\bar{p}$ + H collisions. Analogous to Figs. 5 and 7 for capture by the H atom, typical fits (see Appendixes C and D) of the n and l distributions for capture by the molecule are shown in Figs. 11 and 12. In view of the limited statistics provided by the smaller number of trajectories, the smoothing by the analytic fit is helpful. The simple schemes for the peak and maximum of the distributions, as found for the atomic case, are not applicable here since the quantum numbers are modified by the dynamics and dissociation of an intermediate complex. The results integrated over the energy-dependent capture cross section [see Eq. (22)] are shown in Figs. 13 and 14 in comparison with the results given in Sec. III A for capture by the atom. The n distribution peaks at about 25 instead of $(0.5m_p/m_e)^{1/2}\approx30$, where the peak occurs in the atomic case. Some of this decrease can be ascribed to the larger ionization potential of the molecule, but it is mostly due to the dissociation dynamics. The distribution is narrowed, and the tail is greatly diminished as compared to the atomic case.

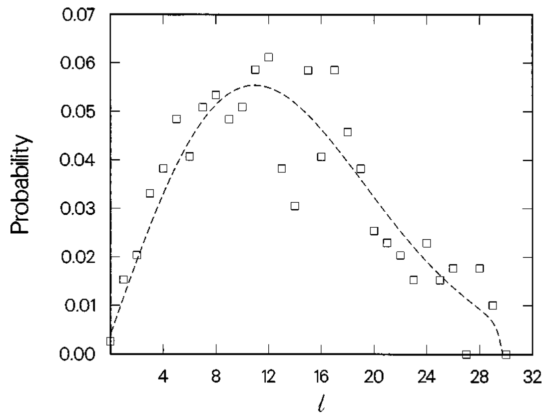

FIG. 12. Distribution of l quantum numbers of $p\bar{p}$ resulting from $\bar{p}$ capture by the H_2 molecule, calculated by the KWC method at energy $E_{\mathrm{c.m.}}=0.20$ a.u. The points are the results of the Monte Carlo trajectories ($\sim$300 contributing), and the dashed curve is a fit (see Appendix B).

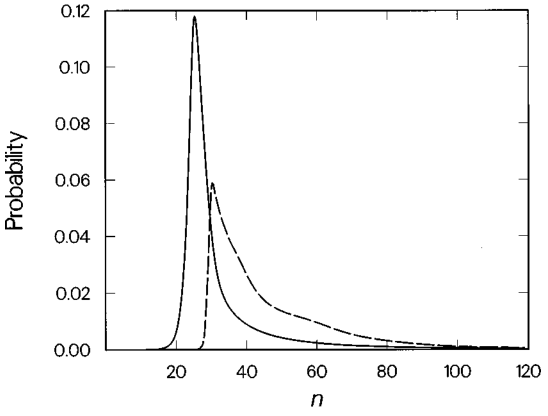

FIG. 13. Distribution of n quantum numbers of $p\bar{p}$ resulting from $\bar{p}$ capture by the H_2 molecule, integrated over collision energies using the KWC results (full curve). For comparison the corresponding result for the H-atom target is shown (dashed curve).

The l distribution resulting from molecular capture is compared with the atomic case in Fig. 14. Again the distribution is shifted toward smaller values. The distribution is also considerably rounded and is no longer dominated by the statistical (proportional to $2l+1$) behavior evident in the atomic case.

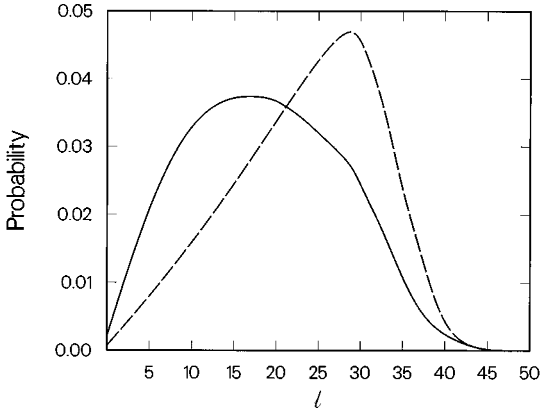

FIG. 14. Distribution of l quantum numbers of $p\bar{p}$ resulting from $\bar{p}$ capture by the H_2 molecule, integrated over collision energies using the KWC results (full curve). For comparison, the corresponding result for the H-atom target is shown (dashed curve).

IV. CONCLUSIONS

The results of $\bar{p}$ capture by the H_2 molecule differ greatly from those for capture by the H atom. The cross sections for both have been calculated using the Kirschbaum-Wilets quasiclassical method extended for accurate treatment of the molecule (this class of methods is known as fermion molecular dynamics). Though such qualitative differences had not been anticipated, they can be understood in the light of cross sections for collisions of normal H^+ with H_2.

The $\bar{p}$ capture has been demonstrated to be affected by the two-center, two-electron molecular structure as well as by the molecular rotational and vibrational dynamics. But the most important effect is due to the vibrational-dissociative dynamics, which enables capture to occur at much higher energies than in collisions with the atom. We should be a bit cautious since the low-lying vibrational states of H_2 are not highly accurate in the quasiclassical treatment, owing to its large vibrational quantum. However, the energy where the effect sets in is the same as that where vibrationally inelastic collisions of H^+ with H_2 are seen experimentally. This correspondence lends credence to the results.

These results are in contrast to those previously found for $\mu^- + H_2$ in a treatment that neglected the ro-vibrational dynamics. In that work [17], the reaction cross sections for H and H_2 targets were of similar magnitude and both cut off sharply above their respective ionization potentials. The close connection with rovibrational excitation suggests that capture by molecules may depend significantly on the molecular isotope and the mass of the incident negative particle. In the future, we plan to use the KWC model to determine if rovibrational dynamics is also important for μ^- capture by H_2 and for $\bar{p}$ capture by D_2.

Since all existing experiments forming $\bar{p}p$ have used molecular targets, the differences between the atom and molecule are highly relevant. At the present time, there would seem to be no purely quantum-mechanical method capable of doing the full five-body reactive dynamics required to solve this problem. On the other hand, the fermion molecular dynamics developed in the present work has been straightforward to apply without further approximations.

ACKNOWLEDGMENTS

This work was stimulated by the Institute for Theoretical Atomic and Molecular Physics 1996 Workshop on Exotic Atoms. The work was performed under the auspices of the U.S. Department of Energy.

APPENDIX A: FITS OF *n* DISTRIBUTIONS

The n quantum-number distributions were fit by the spline form

$$F_n=\begin{cases} be^{\beta n} \quad \text{for } n<n_1 & \text{(A1a)}\\ a\exp\{-[(n-n_0)/\gamma]^2\} \quad \text{for } n_1\leqslant n\leqslant n_2 & \text{(A1b)}\\ c_1/(n-\delta)^3 \quad \text{for } E\geqslant E_1 \quad \text{and } n_2<n\leqslant n_3 & \text{(A1c)}\\ c_2e^{-\beta n} \quad \text{for } E<E_1 \quad \text{and } n_2<n\leqslant n_3 & \text{(A1d)}\\ 0 \quad \text{for } n>n_3, & \text{(A1e)}\end{cases}$$

where the only independent parameters are n_0, γ, β, and δ. n_0 and γ (and a which is renormalized later) were determined by nonlinear least squares, while β and δ were determined by *ad hoc* formulas. The values of n_0 and γ are given in Tables II–IV. The values β and δ were then calculated by

$$\beta=\begin{cases}\max(1000/n_0^2,0.1) \quad \text{for } \bar{p}+\mathrm{H}\ (\mathrm{CTMC})\\ \max(1500/n_0^2,0.1) \quad \text{for } \bar{p}+\mathrm{H}\ (\mathrm{KW})\\ \max(550/n_0^2,0.1) \quad \text{for } \bar{p}+\mathrm{H}_2\ (\mathrm{KWC})\end{cases} \qquad \text{(A2)}$$

and

$$\delta=\begin{cases}30-5800(E-0.5) \quad \text{for } \bar{p}+\mathrm{H}\ (\mathrm{CTMC})\\ 30-3200(E-0.5) \quad \text{for } \bar{p}+\mathrm{H}\ (\mathrm{KW})\\ 18-20(E-0.6) \quad \text{for } \bar{p}+\mathrm{H}_2\ (\mathrm{KWC}).\end{cases} \qquad \text{(A3)}$$

The parameters b, n_1, c_1 or c_2, and n_2 are then determined by continuity conditions (function and first derivative). Thus

$$n_1=n_0-\tfrac{1}{2}\beta\delta^2 \qquad \text{(A4)}$$

and

$$b=a\exp\left[-\left(\frac{n_1-n_0}{\gamma}\right)^2-\beta n_1\right]. \qquad \text{(A5)}$$

For $E\geqslant E_1$,

$$c_1=a(n_2-\delta)^3\exp\left[-\left(\frac{n_2-n_0}{\gamma}\right)^2\right] \qquad \text{(A6)}$$

and

$$n_2=\tfrac{1}{2}\{n_0+\delta+[(n_0+\delta)^2-4n_0\delta+6\gamma^2]^{1/2}\}. \qquad \text{(A7)}$$

For $E<E_1$,

$$c_2=a\exp\left[-\left(\frac{n_2-n_0}{\gamma}\right)^2+\beta n_2\right] \qquad \text{(A8)}$$

and

$$n_2=n_0+\tfrac{1}{2}\beta\gamma^2. \qquad \text{(A9)}$$

The long-range form n^{-3} corresponds to a uniform energy distribution. This distribution can extend to $n\to\infty$ only if $E>E_I$, the ionization potential of the target, since otherwise the remainder of the ionization energy has to come from binding energy of the antiproton to the proton. Thus

$$n_3=\begin{cases}\left(\dfrac{\mu}{2(E_I-E)}\right)^{1/2} \quad \text{for } E<E_I\\ \infty \quad \text{for } E\geqslant E_I.\end{cases} \qquad \text{(A10)}$$

For H_2, the n^{-3} form was found still to yield a better fit for E somewhat below E_I. Thus we took

$$E_1=E_I(\mathrm{H}) \qquad \text{(A11)}$$

for both H and H_2.

Finally the entire fit is renormalized by a common factor N^{-1}, usually close to unity, where N is given by

$$N=N_a+N_b+N_c \qquad \text{(A12)}$$

with

$$N_a=\tfrac{1}{2}\,a\gamma\sqrt{\pi}\left[\Phi\left(\frac{n_2-n_0}{\gamma}\right)-\Phi\left(\frac{n_1-n_0}{\gamma}\right)\right] \tag{A13}$$

(Φ is the error function),

$$N_b=\frac{b}{\beta}(e^{\beta n_1}-1), \tag{A14}$$

and

$$N_c=\begin{cases}\dfrac{1}{2}c[(n_2-\delta)^{-2}-(n_3-\delta)^{-2}] & \text{for } E\geqslant E_1\\[2ex] \dfrac{c}{\beta}(e^{-\beta n_2}-e^{-\beta n_3}) & \text{for } E<E_1.\end{cases} \tag{A15}$$

Fits of the n distributions at energies not calculated were obtained by interpolating the parameters n_0 and γ in Tables II–IV using a monotonically constrained cubic spline [32], and then obtaining the complete fit by the above method.

APPENDIX B: FITS OF l DISTRIBUTIONS

The l distributions were fit by the global functional form

$$F_l=c(2l+1)\exp(bl^k)\exp\left(-\frac{al^2}{(l_1-l)^2}\right), \tag{B1}$$

where $k=1$ for $\overline{p}+\mathrm{H}$ and $k=2$ for $\overline{p}+\mathrm{H}_2$. The fits were done separately (1) for given E summed over n, and (2) for given n integrated over E. In case (1), the procedure was to set $l_1=l_{\max}+1$, where $l_{\max}$ was the largest l seen in capture trajectories at energy E, and determine a, b, and c by nonlinear least squares. In case (2), the procedure was to set $b=0$ and determine a, c, and l_1 by nonlinear least squares.

Fits of the l distributions at energies not calculated were obtained by interpolating the parameters a, b, and l_1 in Tables II–IV using a monotonically constrained cubic spline [32], and then normalizing to obtain the coefficient c.

APPENDIX C: RIGID-ROTOR CONSTRAINT FOR HAMILTON'S EQUATIONS

The rigid-body constraint is enforced by a Lagrange multiplier term in the Hamiltonian. To constrain $r_{bc}=R$, where R is a constant, we use

$$H'=H-\lambda(r_{bc}-R) \tag{C1}$$

where, in terms of the dynamic variables,

$$r_{bc}=|\mathbf{r}_c-\mathbf{r}_b|. \tag{C2}$$

The constrained Hamilton's equations are then

$$\dot{\mathbf{r}}_b=\nabla_{\mathbf{p}_b}H'=\nabla_{\mathbf{p}_b}H, \tag{C3a}$$

$$\dot{\mathbf{r}}_c=\nabla_{\mathbf{p}_c}H'=\nabla_{\mathbf{p}_c}H \tag{C3b}$$

$$\dot{\mathbf{p}}_b=-\nabla_{\mathbf{r}_b}H'=-\nabla_{\mathbf{r}_b}H-\frac{\lambda}{R}(\mathbf{r}_c-\mathbf{r}_b), \tag{C3c}$$

$$\dot{\mathbf{p}}_c=-\nabla_{\mathbf{r}_c}H'=-\nabla_{\mathbf{r}_c}H+\frac{\lambda}{R}(\mathbf{r}_c-\mathbf{r}_b), \tag{C3d}$$

$$\frac{\partial H'}{\partial\lambda}=-(|\mathbf{r}_c-\mathbf{r}_b|-R)=0. \tag{C3e}$$

Note that the form of only the six Hamilton's equations for $\dot{\mathbf{p}}_b$ and $\dot{\mathbf{p}}_c$ is modified by the constraint.

In differential form, constraint (C2) becomes

$$(\mathbf{r}_c-\mathbf{r}_b)\cdot(\dot{\mathbf{r}}_c-\dot{\mathbf{r}}_b)=0, \tag{C4}$$

which, with substitution of Eqs. (C3a) and (C3b), can be written in terms of the dynamic variables as

$$(\mathbf{r}_c-\mathbf{r}_b)\cdot(\nabla_{\mathbf{p}_c}H-\nabla_{\mathbf{p}_b}H)=0. \tag{C5}$$

We now have a set of $3N+1$ equations for N particles in $3N+1$ unknowns including λ. Unfortunately, these equations are not easily put into the generic form $\dot{\mathbf{y}}=f(\mathbf{y})$, and would probably need to be solved by an implicit scheme. However, for the present problem, there is an excellent approximation that still allows our usual solver to work.

The simplification comes from considering the nuclear masses to be infinite, *but only for the calculation of the KWC effective potentials*. Then the gradients are trivial,

$$\nabla_{\mathbf{p}_b}H\rightarrow\frac{1}{m_b}\mathbf{p}_b\,, \tag{C6a}$$

$$\nabla_{\mathbf{p}_c}H\rightarrow\frac{1}{m_c}\mathbf{p}_c\,, \tag{C6b}$$

and the corresponding Hamilton's equations reduce to the usual ones,

$$\dot{\mathbf{r}}_b=\frac{1}{m_b}\mathbf{p}_b, \tag{C7a}$$

$$\dot{\mathbf{r}}_c=\frac{1}{m_c}\mathbf{p}_c\,. \tag{C7b}$$

With this form it is easy to solve for λ. We first rewrite the differential constraints (C5), using Eqs. (C6), as

$$(\mathbf{r}_c-\mathbf{r}_b)\cdot\left(\frac{1}{m_c}\mathbf{p}_c-\frac{1}{m_b}\mathbf{p}_b\right)=0. \tag{C8}$$

By differentiating this equation and using Eqs. (C7), we obtain

$$\left|\frac{1}{m_c}\mathbf{p}_c-\frac{1}{m_b}\mathbf{p}_b\right|^2+(\mathbf{r}_c-\mathbf{r}_b)\cdot\left(\frac{1}{m_c}\,\dot{\mathbf{p}}_c-\frac{1}{m_b}\,\dot{\mathbf{p}}_b\right)=0. \tag{C9}$$

This relation between $\dot{\mathbf{p}}_b$ and $\dot{\mathbf{p}}_c$, together with Eqs. (C3c) and (C3d), then yields an explicit expression for λ,

$$\lambda=\frac{-\left|\frac{1}{m_c}\mathbf{p}_c-\frac{1}{m_b}\mathbf{p}_b\right|^2+(\mathbf{r}_c-\mathbf{r}_b)\cdot\left(\frac{1}{m_c}\nabla_{\mathbf{r}_c}H-\frac{1}{m_b}\nabla_{\mathbf{r}_b}H\right)}{\left(\frac{1}{m_b}+\frac{1}{m_c}\right)R}. \tag{C10}$$

This Lagrange multiplier has an intuitive interpretation. If we identify

$$-\nabla_{\mathbf{r}_b}H\equiv\mathbf{F}_b=\text{ordinary force on nucleus } b, \tag{C11a}$$

$$\frac{1}{m_b}\mathbf{p}_b\equiv\mathbf{v}_b=\text{velocity of nucleus } b, \tag{C11b}$$

$$-\frac{1}{m_b}\nabla_{\mathbf{r}_b}H\equiv\mathbf{a}_b=\text{acceleration of nucleus } b \text{ due to ordinary force}, \tag{C11c}$$

(likewise for nucleus c), and

$$\frac{1}{m_b}+\frac{1}{m_c}\equiv\frac{1}{\mu}\ \ (\mu=\text{reduced mass of } bc), \tag{C11d}$$

$$\mathbf{v}_c-\mathbf{v}_b\equiv\mathbf{v}_{\text{rel}}, \tag{C11e}$$

then

$$\mathbf{v}_{\text{rel}}\cdot\hat{\mathbf{R}}=0 \tag{C12}$$

and

$$\lambda=-\mu[(\mathbf{a}_c-\mathbf{a}_b)\cdot\hat{\mathbf{R}}+v_{\text{rel}}^2/R]. \tag{C13}$$

Thus we can interpret λ as the *constraint force* necessary to balance the centrifugal force and the differential force on nuclei b and c due to forces exerted by all other particles.

We have done calculations to verify that the infinite-nuclear-mass limit for evaluating the KWC potentials is a good approximation. In representative cases, the usual KWC equations were solved again, using this approximation, and the results were hardly changed.

APPENDIX D: RIGID-NONROTOR CONSTRAINT FOR HAMILTON'S EQUATIONS

The rigid nonrotor is defined by the constraint

$$\mathbf{r}_c-\mathbf{r}_b=\mathbf{R}, \tag{D1}$$

where **R** is a constant vector. Though three Lagrange multipliers (a vector) are needed to enforce this condition, the analysis is similar to that of the rigid rotor in Appendix C. We write

$$H'=H-\boldsymbol{\lambda}\cdot(\mathbf{r}_c-\mathbf{r}_b-\mathbf{R}). \tag{D2}$$

The constrained Hamilton's equations are then

$$\dot{\mathbf{r}}_b=\nabla_{\mathbf{p}_b}H'=\nabla_{\mathbf{p}_b}H, \tag{D3a}$$

$$\dot{\mathbf{r}}_c=\nabla_{\mathbf{p}_c}H'=\nabla_{\mathbf{p}_c}H, \tag{D3b}$$

$$\dot{\mathbf{p}}_b=-\nabla_{\mathbf{r}_b}H'=-\nabla_{\mathbf{r}_b}H-\boldsymbol{\lambda}, \tag{D3c}$$

$$\dot{\mathbf{p}}_c=-\nabla_{\mathbf{r}_c}H'=-\nabla_{\mathbf{r}_c}H+\boldsymbol{\lambda}, \tag{D3d}$$

$$\nabla_{\boldsymbol{\lambda}}H'=-(\mathbf{r}_c-\mathbf{r}_b-\mathbf{R})=\mathbf{0}. \tag{D3e}$$

As in Appendix C, we differentiate Eq. (D1) and use Eqs. (D3a) and (D3b) to write it in terms of the dynamic variables,

$$\nabla_{\mathbf{p}_c}H-\nabla_{\mathbf{p}_b}H=\mathbf{0}. \tag{D4}$$

With the infinite-nuclear-mass approximation in the KWC effective potentials, Eq. (D4) implies $(1/m_b)\,\mathbf{p}_b=(1/m_c)\,\mathbf{p}_c$, which can be used in Eqs. (D3c) and (D3d) to obtain an explicit expression for the Lagrange multipliers:

$$\boldsymbol{\lambda}=\frac{\frac{1}{m_c}\nabla_{\mathbf{r}_c}H-\frac{1}{m_b}\nabla_{\mathbf{r}_b}H}{\frac{1}{m_b}+\frac{1}{m_c}}. \tag{D5}$$

---

[1] For a review, see C. J. Batty, Rep. Prog. Phys. **52**, 1165 (1989); for more recent results relating to atomic physics, see Proceedings of the Second Biennial Workshop on Nucleon-Antinucleon Physics (NAN'93), Moscow, 1993 [Phys. At. Nucl. **57**, 1729 (1994)]; Proceedings of the Third International Conference on Nucleon-Antinucleon Physics (NAN'95), Moscow, 1995, [*ibid.* **59**, 1467 (1996)]; Proceedings of the Fourth Biennial Conference on Low-Energy Antiproton Physics (LEAP'96), Dinkelsbühl, Germany, 1996 [Nucl. Phys. B (Proc. Suppl.) **56A**, 69 (1997)].

[2] A. Adamo *et al.*, Phys. Rev. A **47**, 4517 (1993).

[3] P. Hvelplund *et al.*, J. Phys. B **27**, 925 (1994).

[4] M. Agnello *et al.*, Phys. Rev. Lett. **74**, 371 (1995).

[5] H. Knudsen *et al.*, Phys. Rev. Lett. **74**, 4627 (1995).

[6] For an analysis, see G. Schiwietz *et al.*, J. Phys. B **29**, 307 (1996).

[7] M. Iwasaki *et al.*, Phys. Rev. Lett. **67**, 1246 (1991).

[8] E. Widmann *et al.*, Phys. Rev. A **51**, 2870 (1995).

[9] R. S. Hayano *et al.*, Phys. Rev. A **55**, R1 (1997).

[10] B. Ketzer *et al.*, Phys. Rev. Lett. **78**, 1671 (1997).

[11] U. Gastaldi and R. Klapisch, in *From Nuclei to Particles*, edited by A. Molinari (North-Holland, Amsterdam, 1981), p. 462.

[12] J. S. Cohen and G. Fiorentini, Phys. Rev. A **33**, 1590 (1986).

[13] J. S. Cohen, Phys. Rev. A **36**, 2024 (1987).

[14] J. S. Cohen and N. T. Padial, Phys. Rev. A **41**, 3460 (1990).

[15] A. S. Wightman, Phys. Rev. **77**, 521 (1950).

[16] E. Fermi and E. Teller, Phys. Rev. **72**, 399 (1947).

[17] G. Ya. Korenman, Hyperfine Interact. **101/102**, 81 (1996); G. A. Fesenko and G. Ya. Korenman, *ibid.* **101/102**, 91 (1996).

[18] J. S. Cohen, R. L. Martin, and W. R. Wadt, Phys. Rev. A **24**, 33 (1981).

[19] J. D. Garcia, N. H. Kwong, and J. S. Cohen, Phys. Rev. A **35**, 4068 (1987).

[20] N. H. Kwong, J. D. Garcia, and J. S. Cohen, J. Phys. B **22**, L633 (1989).

[21] J. S. Cohen, Phys. Rev. A **27**, 167 (1983).

[22] Comput. Phys. Commun. **63** (1991), special issue on time-dependent methods for quantum dynamics, edited by K. C. Kulander.

[23] C. L. Kirschbaum and L. Wilets, Phys. Rev. A **21**, 834 (1980).

[24] J. S. Cohen, Phys. Rev. A **51**, 266 (1995).

[25] J. S. Cohen, Phys. Rev. A **54**, 573 (1996).

[26] W. A. Beck and L. Wilets, Phys. Rev. A **55**, 2821 (1997).

[27] W. A. Beck, L. Wilets, and M. A. Alberg, Phys. Rev. A **48**, 2779 (1993).

[28] L. de Broglie, Philos. Mag. **47**, 446 (1924).

[29] J. S. Cohen, in *Electromagnetic Cascade and Chemistry of Exotic Atoms*, edited by L. M. Simons *et al.* (Plenum, New York, 1990), p. 1.

[30] M. Leon, Phys. Rev. A **17**, 2112 (1978).

[31] A. V. Phelps, J. Phys. Chem. Ref. Data **19**, 653 (1990).

[32] J. M. Hyman, SIAM (Soc. Ind. Appl. Math.) J. Sci. Stat. Comput. **4**, 645 (1983).